

# Weak Lensing by Minifilament or Minivoid as the Origin of Flux-ratio Anomalies in Lensed Quasar MG0414+0534

Kaiki Taro Inoue<sup>1\*</sup>

<sup>1</sup>*Department of Science and Engineering, Kinki University, Higashi-Osaka, 577-8502, Japan*

9 May 2019

## ABSTRACT

We explore the weak lensing effects by ministructures in the line-of-sight in a quadruply lensed quasar MG0414+0534 that shows an anomaly in the flux ratios. We find that the observed flux-ratio anomaly can be explained by a presence of either a minifilament or a minivoid in the line-of-sight with a surface mass density of the order of  $10^{8-9} h^{-1} M_{\odot}/\text{arcsec}^2$  without taking into account any subhalos in the lensing galaxy. The astrometric perturbation by a possible minifilament/minivoid at the primary lens plane is  $\lesssim 0.001$  arcsec and the amplitudes of convergence perturbations due to these perturbers are  $\delta\kappa \sim 0.004 - 0.008$  at the place of an image that shows anomaly. In order to discriminate models with the line-of-sight ministructures from those with a subhalo(s) in the lensing galaxy, we need to precisely measure the projected convergence and shear perturbations around the lensing galaxy. The differential magnification effect could break the model degeneracy if the source size is  $\gtrsim 100$  pc. Observation at the submillimeter band using interferometers will enable us to determine the origin of anomalies in the flux ratios.

**Key words:** galaxies: formation - cosmology: theory - gravitational lensing - dark matter.

## 1 INTRODUCTION

The physics of non-linear clustering on scales of  $\lesssim 1$  Mpc has not been well understood. First, the observed density profiles of dwarf galaxies are shallower than the values predicted from  $N$ -body simulations, which is called the ‘cusp-core problem’ (Navarro et al. 1996; Moore et al. 1999; Swaters et al. 2003; Simon et al. 2005). Second, the number of observed satellite galaxies in our Galaxy is significantly smaller than the predicted value, which is known as the ‘missing satellites problem’ (Klypin et al. 1999; Moore et al. 1999). Third, the observed circular velocities of most massive subhalos in our Galaxy are also significantly smaller than the predicted values, which is called the ‘too big to fail problem’ (Boylan-Kolchin et al. 2011; Wang et al. 2012).

In order to address these issues, it is important to constrain the number density of dark satellites in extragalactic halos. It has been known that some quadruply lensed quasars show anomalies in the observed flux ratios of lensed images provided that the gravitational potential of the lens is sufficiently smooth. Such a discrepancy is called the ‘anomalous flux ratio’ and has been considered as an imprint of cold dark matter (CDM) subhalos with a mass of  $\sim 10^{8-9} M_{\odot}$  in lensing galaxies (Mao & Schneider 1998; Metcalf & Madau

2001; Chiba 2002; Dalal & Kochanek 2002; Keeton et al. 2003; Metcalf et al. 2004; Chiba et al. 2005; Sugai et al. 2007; McKean et al. 2007; More et al. 2009; Minezaki et al. 2009; Xu et al. 2009, 2010).

However, intergalactic halos in the line-of-sight may act as perturbers as well (Chen et al. 2003; Metcalf 2005; Xu et al. 2012). Indeed, taking into account the astrometric shifts, recent studies have found that the observed anomalous flux ratios can be explained solely by these line-of-sight structures with a surface density  $\sim 10^{7-8} h^{-1} M_{\odot}/\text{arcsec}^2$  (Inoue & Takahashi 2012; Takahashi & Inoue 2014; Inoue et al. 2014) without taking into account subhalos in the lensing galaxies. The observed increase in the amplitude of magnification perturbations as a function of the source redshift strongly implies that the origin is associated with sources rather than lenses.

In order to determine the origin of flux-ratio anomalies, we need to precisely measure the perturbation of gravitational potential projected on a plane perpendicular to the line-of-sight. If it is caused by a subhalo in the lensing galaxy halo, then the perturbation effect is limited to the region around the perturber. Even if the perturbation is caused by a number of subhalos in the lensing galaxy, we may be able to neglect the spatial correlation of between perturbers, as

\* E-mail: kinoue@phys.kindai.ac.jp

structures such as filaments and walls can be easily destroyed due to tidal force in the potential of the parent halo<sup>1</sup>.

On the other hand, if the perturbation is caused by objects in the line-of-sight, the spatial correlation between perturbers may be important than previously thought. In the CDM scenarios, the cosmic web structures appear on all the scales that exceed the free-streaming scale. Therefore, any clumps formed on walls and filaments should have spatial correlations between them. Moreover, inter-galactic medium may reside along these structures and enhance the lensing effect by these clumps due to radiative cooling. In fact, recent studies on Lyman- $\alpha$  emission and high-velocity clouds around the Milky Way suggest an existence of substantial cold gas accreted on filaments (on scales  $< 1$  Mpc) of the ancient cosmic web (Dekel et al. 2009; Cantalupo et al. 2014; Martin et al. 2014). These spatially extended objects (filaments or walls) can perturb the fluxes of lensed images if they are common in the universe.

In the following, we call them “ministruclures” if the typical length-scale of these structures (dark matter + baryon) is just  $\sim 10 - 100$  kpc (Inoue & Takahashi 2012), which is significantly smaller than those (on scales of  $10 - 100$  Mpc) usually discussed in literature (Colberg et al. 2005; Mead et al. 2010; Higuchi et al. 2014).

In this paper, we investigate whether the flux-ratio anomaly in an anomalous quadruple lens MG0414+0534 can be explained by a minivoid or a minifilament in the line-of-sight and study whether we can break the model degeneracy. For simplicity, we put a perturber at the primary lens plane where the deflection angle is relatively large (Inoue & Takahashi 2012). Although, the objects in the line-of-sight may have complex structures, we use simple toy models to arrive at some quick and dirty results. Since the gravitational effects of non-linear ministruclures are different from subhalos, we may be able to distinguish between them by measuring the differential magnification effect provided that the source size is sufficiently large. In section 2, we present the observational data of MG0414+0534. In section 3, we describe a simple lens model of a tidally truncated singular isothermal sphere (SIS), a compensated homogeneous filament and void. In section 4, we show our results of  $\chi^2$  fitting and the gravitational effect in models with a minifilament/minivoid. In section 5, the differential magnification effect in minifilament/minivoid models is discussed. In section 6, we summarize our result and discuss some relevant issues and future prospects.

In what follows, we assume a cosmology with a matter density  $\Omega_{m,0} = 0.3134$ , a baryon density  $\Omega_{b,0} = 0.0487$ , a cosmological constant  $\Omega_{\Lambda,0} = 0.6866$ , a Hubble constant  $H_0 = 67.3$  km/s/Mpc, a spectral index  $n_s = 0.9603$ , and the root-mean-square (rms) amplitude of matter fluctuations at  $8h^{-1}$  Mpc,  $\sigma_8 = 0.8421$ , which are obtained from the observed CMB (Planck+WMAP polarization; Planck Collaboration et al. (2013)).  $G$  and  $c$  denote the gravitational constant and speed of light, respectively.

<sup>1</sup> If tidal streams in galaxy halos persist for long time, they might mimic the lensing effects by filaments in the intergalactic space.

## 2 MG0414+0534

The fold-caustic lens MG0414+0534 consists of two bright images A1, A2 and two faint images B, C. The images A1 and B are minima, and A2 and C are saddles. A source quasar at  $z_S = 2.64$  is lensed by an elliptical galaxy (hereinafter referred to as G) at  $z_L = 0.96$  (Hewitt et al. 1992; Lawrence et al. 1995; Tonry & Kochanek 1999). A simple lens model, a singular isothermal ellipsoid (SIE) (Kormann et al. 1994) with an external shear (ES) cannot fit the image positions as well as the flux ratios. Schechter & Moore (1993) and Ros et al. (2000) suggested that another galaxy is necessary for fitting the relative image positions. As shown in table 1, we use the MIR flux ratios A2/A1 and B/A1 obtained from measurements by Minezaki et al. (2009) and MacLeod et al. (2013), since the radio fluxes might be hampered by Galactic refractive scintillation (Koopmans et al. 2003). For the astrometry, we use the data from CASTLES data base. However, in our analysis, we do not use the VLBI data (Ros et al. 2000; Trotter et al. 2000) as there is an ambiguity in identifying components of jets and estimating the position errors due to large shear at the places of lensed images.

Although, the observed image positions are well fitted by an SIE and an external shear (SIE-ES) plus an SIS at the lens redshift  $z_l$ , that accounts for object X, the flux ratios are not well fitted. A possible subhalo near A2 significantly improves the fit (Minezaki et al. 2009; MacLeod et al. 2013). The orientation of the external shear is in the same general direction as another object G6 found  $4.''4$  southwest of image C in the HST H-band image but it is not massive enough to fully account for the external shear (MacLeod et al. 2013).

In this paper, we use a model that consists of an SIE (for G) plus an external shear (for environment), and an SIS (for X) whose predicted positions of lensed images and centroids of galaxies are fitted to the observed data. We do not use the data of relative fluxes of lensed images for estimating the unperturbed model. The flux ratios are used for parameter fitting when a perturber (subhalo/filament/void) is taken into account.

## 3 LENS MODEL

For simplicity, as a perturber, we consider three types of models: a tidally truncated SIS halo, a compensated homogeneous filament and a compensated homogeneous void. Because of mass compensation, the gravitational potential of a perturber vanishes at the outer boundary in the latter two cases. Any locally uncompensated filaments (voids) can be modelled by adjusting the size of the outer positive (negative) region.

### 3.1 Subhalo

As a simple model of subhalo in the primary lensing galaxy, we consider a tidally truncated SIS (hereinafter referred to as tSIS). At a distance  $R$  from the center of the primary lensing galactic halo with a one-dimensional velocity dispersion  $\sigma_0$ , the tidal radius  $R_t$  (proper length) is approximately

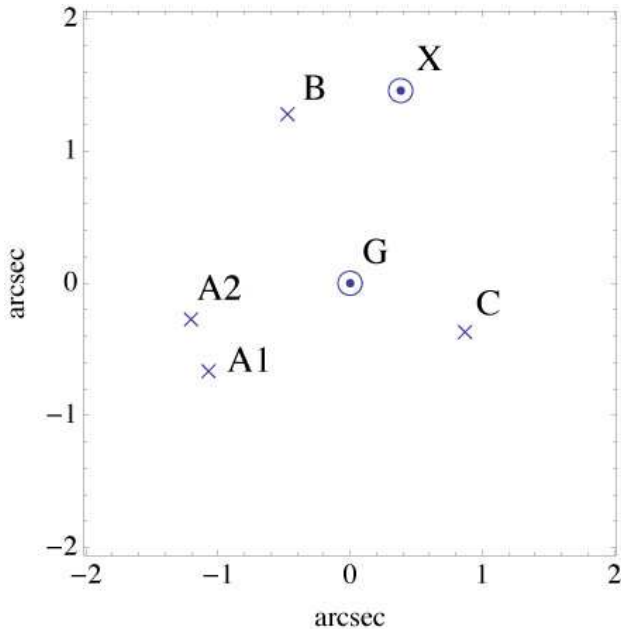


**Figure 1.** The gravitational lens system MG0414+0534 (plots of data in table 1).

**Table 1.** The observed HST positions of lensed images (A1,A2,B,C) and the centroids of the primary lens G and object X and the MIR flux ratios in MG0414+0534.

Image	Position(arcsec)	MIR flux ratio(obs.)
A1	$(-1.07 \pm 0.003, -0.667 \pm 0.003)$	
A2	$(-1.203 \pm 0.003, -0.274 \pm 0.003)$	A2/A1=0.919 $\pm$ 0.021
B	$(-0.474 \pm 0.000, 1.276 \pm 0.000)$	B/A1=0.347 $\pm$ 0.013
C	$(0.871 \pm 0.003, -0.372 \pm 0.003)$	
G	$(0.000 \pm 0.003, 0.000 \pm 0.003)$	
X	$(0.383 \pm 0.011, 1.457 \pm 0.009)$	

Note: The positions are taken from CASTLES data base (Falco et al. (1997)) and are relative to image G. The MIR flux ratios are taken from the combined results of Minezaki et al. (2009) and MacLeod et al. (2013).

given by  $R_t \approx R\sigma/\sigma_0$  where  $\sigma$  is the one-dimensional velocity dispersion of a tSIS. In terms of the Einstein radius (mass scale)  $b_h$  of a tSIS and that of an SIS for a parent galaxy halo  $b_0$ , the tidal radius can be written as  $R_t = R\sqrt{b_h/b_0}$ .

In what follows, we assume that the tSIS resides at the lens plane for simplicity. In this case,  $R$  coincides with the angular distance between the center of the primary lens and that of a tSIS. In general, however, the tidal radius can be larger than the value in which a tSIS resides at the lens plane for a given angular distance from the center of the primary lens. The deflection angle  $\hat{\alpha}_h$  is constant inside but it decays as  $\hat{\alpha}_h \propto 1/R$  outside the tidal radius.

### 3.2 Compensated homogeneous filament

We consider an infinitely long filament that has a positive constant density  $\rho_+$  inside a radius  $R_+$  (region I) and a negative constant density  $\rho_- < 0$  at  $R_+ < R < R_-$  (region

II), where  $R$  denotes the proper distance from the axis. At  $R > R_-$  (region III),  $\rho = 0$  (Fig. 1). From the compensating condition, we have

$$\rho_- = -\frac{\rho_+ R_+^2}{R_-^2 - R_+^2}. \quad (1)$$

If we set the gravitational potential at region III equal to zero, i.e.,  $\psi_{III}(R) = 0$ , potentials at region I and II are

$$\psi_I(R) = \pi G \rho_+ \left[ (R^2 - R_+^2) + \frac{2R_+^2}{R_-^2 - R_+^2} \left( R_-^2 \ln \frac{R_+}{R_-} - \frac{R_+^2 - R_-^2}{2} \right) \right], \quad (2)$$

and

$$\psi_{II}(R) = \frac{2\pi G \rho_+ R_+^2}{R_-^2 - R_+^2} \left[ R_-^2 \ln \frac{R}{R_-} - \frac{R^2 - R_-^2}{2} \right]. \quad (3)$$

Integrating the gravitational potential  $\psi(\mathbf{R}_\perp, Z)$  at  $-\infty < Z < \infty$  where  $\mathbf{R}_\perp = (X, Y)$  are the orthogonal proper coordinates at the lens plane and  $z$  is the proper coordinate along the line-of-sight, and taking the gradient, we have the X-component of the deflection angle  $\hat{\alpha}_f$  at  $\mathbf{R}_\perp = (X, Y)$ ,

$$\hat{\alpha}_f = b_f \times \begin{cases} 0, & R_- \leq |\mathbf{R}_\perp| \\ \frac{1}{R_-^2 - R_+^2} \left[ -X \sqrt{R_-^2 - X^2} + R_-^2 \tan^{-1} \left( \frac{\sqrt{R_-^2 - X^2}}{X} \right) \right], & R_+ < |\mathbf{R}_\perp| < R_- \\ \frac{1}{R_-^2 - R_+^2} \left[ -X \sqrt{R_-^2 - X^2} + 2X \sqrt{R_+^2 - X^2} + R_-^2 \tan^{-1} \left( \frac{\sqrt{R_-^2 - X^2}}{X} \right) - R_-^2 \tan^{-1} \left( \frac{\sqrt{R_+^2 - X^2}}{X} \right) \right], & 0 \leq |\mathbf{R}_\perp| < R_+, \end{cases} \quad (4)$$

where  $b_f$  describes the mass scale, which is given by

$$b_f \equiv \frac{8\pi G R_+^2 \rho_+}{c^2}. \quad (5)$$

In terms of linear density  $\lambda$ ,  $\theta_f$  can be also written as

$$b_f = \frac{8G\lambda}{c^2}. \quad (6)$$

Because the filament is axi-symmetric, Y-component of the deflection angle  $\hat{\alpha}_f$  is zero. The deflection angle  $\hat{\alpha}_f$  as a function of  $X/R_+$  is shown in Fig. 3.

### 3.3 Compensated homogeneous void

For simplicity, we consider homogeneous spherical voids that are compensated in mass. We assume that they have a negative constant density  $\rho_-$  inside a radius  $R_-$  (region I) and a positive constant density  $\rho_+$  at  $R_+ < R < R_-$  (region

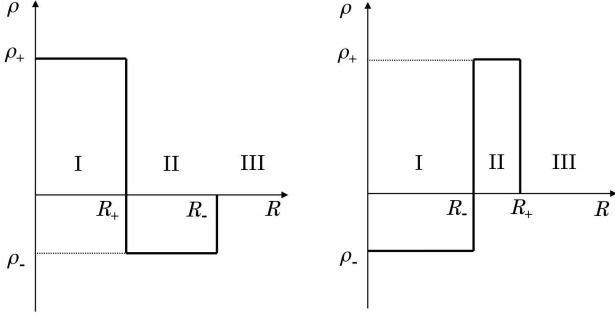


**Figure 2.** Mass density of a compensated filament (left) and that of a compensated void (right).

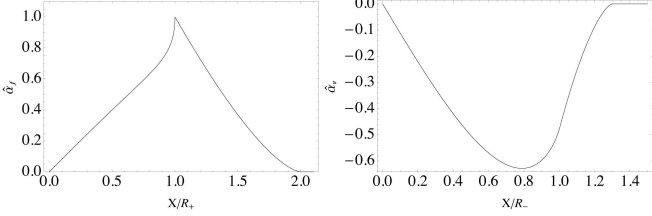


**Figure 3.** Deflection angle of a compensated filament (left) and that of a compensated void (right)

II), where  $R$  denotes the proper distance from the center of a void. At  $R > R_+$  (region III), the density is vanishing, i.e.,  $\rho = 0$  (Fig. 1). The mass deficient at  $R < R_-$  is  $M_v = 4\pi\rho_-R_-^3/3$ . Then, the  $X$ -component of the deflection angle  $\hat{\alpha}_v$  at  $\mathbf{R}_\perp = (X, Y = 0)$  in the lens plane is (Amendola et al. 1999),

$$\hat{\alpha}_v = b_v \times \begin{cases} 0, & R_+ \leq |\mathbf{R}_\perp| \\ \tilde{X}^{-1}(\tilde{d}^3 + 3\tilde{d}^2 + 3\tilde{d})^{-1} \\ \quad \times [(1 + \tilde{d})^2 - \tilde{X}^2]^{3/2}, & R_- < |\mathbf{R}_\perp| < R_+ \\ \tilde{X}^{-1}(\tilde{d}^3 + 3\tilde{d}^2 + 3\tilde{d})^{-1} \\ \quad \times [(1 + \tilde{d})^2 - \tilde{X}^2]^{3/2} \\ \quad - (1 + \tilde{d})^3(1 - \tilde{X}^2)^{3/2}, & 0 \leq |\mathbf{R}_\perp| < R_-, \end{cases} \quad (7)$$

where  $\tilde{X} \equiv X/R_-$ ,  $\tilde{d} \equiv R_+/R_- - 1$ , and  $b_v$  describes the mass scale, which is given by

$$\begin{aligned} b_v &\equiv \frac{4GM_v}{c^2 R_-} \\ &= \frac{16\pi GR_v^2 \rho_-}{3c^2}. \end{aligned} \quad (8)$$

The  $Y$ -component of  $\hat{\alpha}_v$  is zero for  $Y = 0$ . For  $Y \neq 0$ , a rotation of coordinates by an angle  $\phi = \tan^{-1}(Y/X)$  gives the deflection angle  $\hat{\alpha}_v = (\hat{\alpha}_v, 0)$  as the void is spherically symmetric. The reduced deflection angle  $\alpha_v$  as a function of  $X/R_-$  is shown in Fig. 3.

## 4 SIMULATION

For simplicity, we consider models that consist of an SIE-ES (G) plus an SIS (X) perturbed by either a tidally cut

SIS, a compensated filament, or a compensated void. The parameters of the SIE-ES is the mass scale  $b_G^2$ , the position of the primary lens  $(x_G, y_G)$ , the ellipticity  $e(G)$ , the external shear  $\gamma$ , and their angles,  $\phi_{e(G)}$ ,  $\phi_\gamma$  measured in East of North. The parameters of SIS is the Einstein radius (mass scale)  $b_X$  and the position  $(x_X, y_X)$ . The parameters of perturbers are the positions  $(x_h, y_h)$ ,  $(x_f, y_f)$ ,  $(x_v, y_v)$  and the mass scales  $b_h, b_f, b_v$  for the subhalo, filament and void models, respectively.  $(x_h, y_h)$  and  $(x_v, y_v)$  correspond to the centers of circular symmetry in a subhalo and a void, respectively.  $(x_f, y_f)$  denotes the position on the axis of a filament that is closest to the center of the primary lens. The extent of filament and void are specified by  $R_+$  and  $R_-$  (see section 3 for definition). The position of a source is denoted as  $(x_s, y_s)$ .

As an unperturbed model, we adopt an SIE-ES plus an SIS and use only observed positions of lensed images and centroids of lensing galaxies for fitting. We assume that the gravitational potential of the primary lens is sufficiently smooth on the scale of the Einstein radius of the primary lens and the fluxes of lensed images are perturbed by a perturber whose gravitational potential varies on scales smaller than the Einstein radius. We do not use observed fluxes as they would significantly distort the unperturbed gravitational potential. For perturbed models, however, we use the MIR flux ratios of lensed images as well as the observed positions. For simplicity, we assume that object X and a possible perturber reside at the lens plane.

We assume weak priors for the ellipticity  $e$  and the external shear  $\gamma$  for the primary lens galaxy G such that  $e = 0.2 \pm 0.2$  and  $\gamma = 0.1 \pm 0.1$ . The expected value of ellipticity  $e$  is taken from the elliptical isophotes of HST images (Falco et al. 1997). The mean and  $1-\sigma$  error of external shear  $\gamma$  is obtained from quadruple lenses observed at the MIR band (Takahashi & Inoue 2014).

For the unperturbed model, we find that  $\chi^2$  for the images and the primary lens positions is extremely good as  $\chi_{\text{pos}}^2 = 0.006$  (table 2). This is not surprising as the degree of freedom is zero if one does not impose the weak priors on the ellipticity and external shear<sup>3</sup>. However,  $\chi^2$  for the fluxes are poor as  $\chi_{\text{flux}}^2 = 37.2$ . The best-fit flux ratio  $A2/A1 = 1.038$  is consistent with the prediction of the fold-caustic relation  $A2/A1 = 1$  with an error of  $\sim 4\%$ , but it is deviated from the observed value  $A2/A1 = 0.919 \pm 0.021$  by  $\sim 12\%$ .

In order to reduce the number of model parameters, we adopt the following assumptions: 1) In the subhalo model, the tidal radius of an SIS is given by  $\theta_t = \sqrt{b_h/b_G}$ , where  $b_h$  and  $b_G$  are the Einstein radii of an SIS and an SIE, respectively. This approximation can be verified if the subhalo resides near A2 in the lens plane as the angular distance between A2 and G is  $1.234 \sim 1 \text{ arcsec}$ . 2) In the filament model, the typical deflection angle due to a filament is assumed to be  $b_f = 0.003 \text{ arcsec}$  and the filament is perpendicular to the line-of-sight. 3) In the void model, we assume that  $R_- = b_G$  and  $R_+ = 1.3 b_G$ . This assumption can be verified as follows. If the radius of a void is significantly larger than  $b_G$ ,

<sup>2</sup>  $b_G$  corresponds to the Einstein radius  $\theta_E$  of an SIS whose mass inside  $\theta_E$  is equal to the mass inside the critical curve of an SIE (Kormann et al. 1994).

<sup>3</sup> The small  $\chi_{\text{pos}}^2$  may suggest that the actual errors of obtained positions are much smaller than the estimated values.

the density perturbation mainly contributes to the constant convergence and shear of the unperturbed lens. If smaller than  $b_G$ , the contribution of line-of-sight structures to convergence is expected to decrease (Inoue & Takahashi 2012) in comparison with larger structures. The width of a wall of stacked voids with a radius  $\sim 20 - 50 h^{-1} \text{Mpc}$  is expected to be equal to or less than the radius (Sutter et al. 2014). However, on much smaller scales ( $\lesssim 5 - 10 h^{-1} \text{kpc}$ ), there have been no results yet. As a working hypothesis, we assume that the width of the wall is one third of the void radius, i.e.,  $d = 0.3$ . Although our assumption seems too restrictive, we can construct similar models with a different width of wall by a scale transformation provided that a lensed image lies near the edge of the wall and the width is sufficiently thin, i.e.,  $\tilde{d} \ll 1$ . Suppose that a lensed image X lies at a distance  $1 + d - \varepsilon$ ,  $\varepsilon > 0$  from the center of a void. Assuming  $\varepsilon \ll d \ll 1$ , equation (7) gives the approximated deflection angle  $\hat{\alpha}_v \approx (\theta_\varepsilon \tilde{X}, \theta_\varepsilon \tilde{Y})$ , where

$$\theta_\varepsilon = \frac{-2\sqrt{2}b_v\varepsilon^{3/2}}{3d} + O(\varepsilon^{5/2}) + \dots \quad (9)$$

Thus, at the lowest order in  $\varepsilon$ , the deflection angle  $\hat{\alpha}_v$  is invariant under a scale transformation  $d \rightarrow \lambda d$  and  $b_v \rightarrow \lambda b_v$ , where  $\lambda$  is a constant.

As shown in table 2, we find that the  $\chi^2$  fit for our compensated void model ( $\chi^2_{\text{tot}}/\text{dof} = 1.5$ ) and filament model ( $\chi^2_{\text{tot}}/\text{dof} = 2.6$ ) are better than that for the subhalo model ( $\chi^2_{\text{tot}}/\text{dof} = 2.8$ ). This result suggests that our void and filament models may explain the observed anomalies in MG0514+0534 as well as the subhalo model. As shown in Fig. 4, we find that A2 is close to the filament and the wall of the void in the best-fit models. This suggests that the flux-ratio anomaly may be caused by a positive density perturbation in the neighbourhood of A2.

We find that the truncated angular radius of the tSIS (corresponding to  $R_t$ ) in the best-fit model is 0.048 arcsec and the mean perturbation of convergence within  $R_t$  is 0.048 (Fig. 5). The mass inside  $R_t$  is  $7 \times 10^8 h^{-1} M_\odot$ . The angular distance between the center of the tSIS and A2 is  $d(\text{A2}) = 0.13$  arcsec. In the best-fit filament model, it turns out that the surface density and the line density of the positive density region are  $8 \times 10^8 h^{-1} M_\odot/\text{arcsec}^2$  and  $2 \times 10^8 h^{-1} M_\odot/\text{arcsec}$ , respectively. The perturbation of convergence at A2 is  $\delta\kappa \approx 0.008$ . In the best-fit void model, the mass deficit is turned out to be  $5 \times 10^9 h^{-1} M_\odot$  and the surface densities of negative and positive density regions are  $-4 \times 10^9 h^{-1} M_\odot/\text{arcsec}^2$  and  $6 \times 10^9 h^{-1} M_\odot/\text{arcsec}^2$ , respectively. The perturbation of convergence at A2 is  $\delta\kappa \approx 0.004$ . Thus, the order of the surface density of a possible filament/void is  $10^{8-9} h^{-1} M_\odot/\text{arcsec}^2$ , which can be called ‘‘ministruktures’’. Within  $b_G$ , the corresponding typical mass scale is  $10^{8-9} h^{-1} M_\odot$ .

One might notice that the amplitude of the obtained surface density ( $\sim 10^4$  times the mean cosmological mass density) is too big in the negative density regions. However, we need to remember that the obtained surface mass density corresponds to the sum of contributions from the primary lens and the line-of-sight structures, which cannot be separated observationally. Therefore, if some portion of a constant convergence is subtracted from the best-fit SIE-ES model, and added to the line-of-sight perturbers, such negative density regions can be compensated by positive mass.

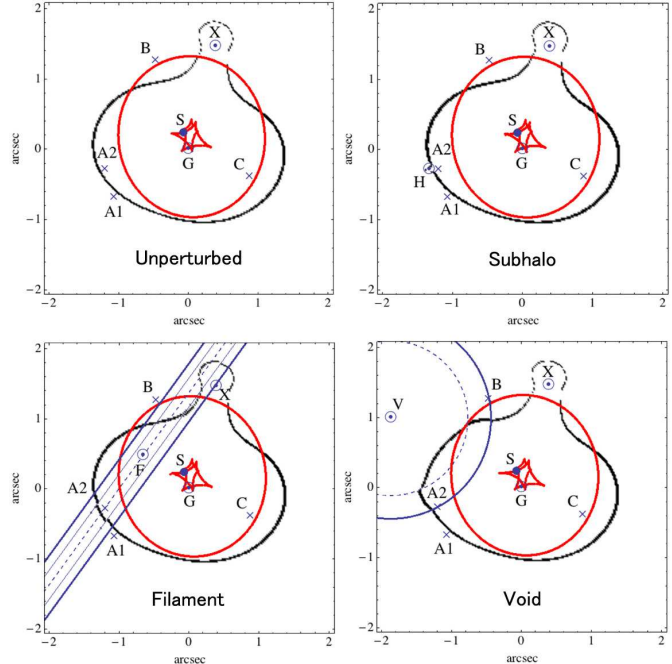


**Figure 4.** Caustics (red) and critical curves (black) for the unperturbed and perturbed best-fit models. H, F, and V correspond to the centers of a subhalo, a filament, and a void, respectively. S is the position of a point source in each best-fit model. G denotes the position of the observed centroid of the primary lensing galaxy. X represents the position of the centroid of object X, possibly a satellite galaxy. The central axis of the filament is shown by a dashed line. The boundaries of positive and negative density regions for the filament(void) model are denoted by thin(thick) and thick(thin) blue lines(curves).

The three models show different patterns of convergence perturbation at the scale  $b_G$  of the primary lens. In other words, it implies that we can break the degeneracy of these models by looking at global patterns of gravitational perturbations to the primary lens.

The typical amplitudes of perturbations in deflection angles at the places of the lensed images are small as  $\delta\alpha \lesssim 0.001$  arcsec (Fig. 6). Therefore, the observational errors in positions of optical images ( $O(10^{-3})$  arcsec) still admit a variety of lens models that predict similar flux ratios within the relative errors of  $\lesssim 0.01$ .

In order to check this point, we calculate the magnification perturbations caused by perturbers. Indeed, we find similar magnification perturbations at the place of A2 for all the three models. However, the patterns of magnification perturbations turn out to be different at other places. This is due to the difference in convergence and shear on scales  $\lesssim b_G$ . Therefore, we may be able to break the degeneracy by measuring the differential magnifications, which will be discussed in the next section.

**Table 2.** Best-fit model parameters for MG0414+0534

Model	Unperturbed	Subhalo	Filament	Void
$b_G(\prime\prime)$	$1.103 \pm 0.001$	$1.103 \pm 0.001$	$1.103 \pm 0.001$	$1.1033 \pm 0.0008$
$(x_s, y_s)(\prime\prime)$	$(-0.0696, 0.2371)$	$(-0.0690, 0.2372)$	$(-0.0694, 0.2370)$	$(-0.0695, 0.2368)$
$e(G)$	$0.231 \pm 0.001$	$0.231 \pm 0.002$	$0.231 \pm 0.001$	$0.231 \pm 0.001$
$\phi_{e(G)}(\text{deg})$	$-82.2 \pm 0.1$	$-82.22 \pm 0.05$	$-82.2 \pm 0.1$	$-82.2 \pm 0.1$
$\gamma$	$0.1010 \pm 0.0004$	$0.1010 \pm 0.0002$	$0.1010 \pm 0.0004$	$0.1010 \pm 0.0003$
$\phi_\gamma(\text{deg})$	$53.9 \pm 0.1$	$53.93 \pm 0.05$	$53.9 \pm 0.1$	$53.9 \pm 0.1$
$(x_G, y_G)(\prime\prime)$	$(0.0000, -0.0001)$	$(0.0007, 0.0000)$	$(0.0000, -0.0001)$	$(0.0002, -0.0002)$
$b_X(\prime\prime)$	$0.184 \pm 0.001$	$0.184 \pm 0.003$	$0.184 \pm 0.001$	$0.184 \pm 0.001$
$(x_X, y_X)(\prime\prime)$	$(0.383 \pm 0.008, 1.457 \pm 0.008)$	$(0.383 \pm 0.009, 1.457 \pm 0.009)$	$(0.383 \pm 0.008, 1.457 \pm 0.008)$	$(0.383 \pm 0.008, 1.456 \pm 0.008)$
$b_h(\prime\prime)$	$0.002537 \pm 0.000008$			
$(x_h, y_h)(\prime\prime)$	$(-1.34 \pm 0.02, -0.29 \pm 0.02)$			
$b_f(\prime\prime)$	$0.003(\text{fixed})$			
$(x_f, y_f)(\prime\prime)$	$(-0.66 \pm 0.02, 0.48 \pm 0.02)$			
$b_v(\prime\prime)$	$0.035 \pm 0.002$			
$(x_v, y_v)(\prime\prime)$	$(-1.869 \pm 0.006, 0.990 \pm 0.003)$			
$R_+(\prime\prime)$			$0.12^{+0.03}_{-0.02}$	$1.3 b_G(\text{fixed})$
$R_-(\prime\prime)$			$R_+(\text{fixed})$	$b_G(\text{fixed})$
$\chi_{\text{pos}}^2$	0.006	0.68	0.01	0.07
$\chi_{\text{flux}}^2$	37.2	4.87	5.09	2.96
$\chi_{\text{weak}}^2$	0.024	0.024	0.024	0.024
$\chi_{\text{tot}}^2/\text{dof}$	37/2	5.6/2	5.1/2	3.0/2
A2/A1	1.038	0.926	0.920	0.920
B/A1	0.328	0.334	0.328	0.347

Note:  $\chi_{\text{tot}}^2$  is the sum of contributions from the image and lens positions ( $\chi_{\text{pos}}^2$ ), the flux ratios ( $\chi_{\text{flux}}^2$ ), and the weak priors ( $\chi_{\text{weak}}^2$ ) on  $e(G)$  and  $\gamma$ . The parameter uncertainties were estimated from the range over which  $\Delta\chi_{\text{tot}}^2 \leq 1$  as each parameter was varied and the other parameters were fixed at optimised values except for the source position. The uncertainties of the primary lens positions are not listed as they are well below the numerical accuracy.

## 5 DIFFERENTIAL MAGNIFICATION EFFECT

As shown in Fig. 7, the perturbation of magnification at the positions of lensed images are similar in all the models. However, the global pattern of perturbation differs in each case. In order to discriminate the three models, we consider the differential magnification effect. For simplicity, as the surface brightness of an extended source, we assume a circular Gaussian profile centred at the best-fit position of a point source. The source radius  $r$  is represented by the standard deviation  $\sigma$ . As one can see in Fig. 8, the flux ratios vary as a function of a source radius  $r$ . The flux ratios of the void model and the subhalo model differ by 5 ~ 50% for

$0 < r < 400$  pc. On the other hand, the difference between the filament model and the subhalo model is only 1 ~ 2% except for  $r \sim 100$  pc (see Fig. 8). This is because that the pattern of magnification perturbations of the filament and the subhalo model are similar in the neighbourhood of A1 and A2. However, if the position of the extended source is not centred at the position of the best-fit point source, we may detect a noticeable change if the lensed image in the neighbourhood of B crosses the filament. The red-blue decomposition of line emission may work for this purpose.

With errors of the order of  $< 0.1$  per cent in the flux ratios and  $< 0.1$  arcsec in the angular resolution, we can discriminate the possible models that can account for

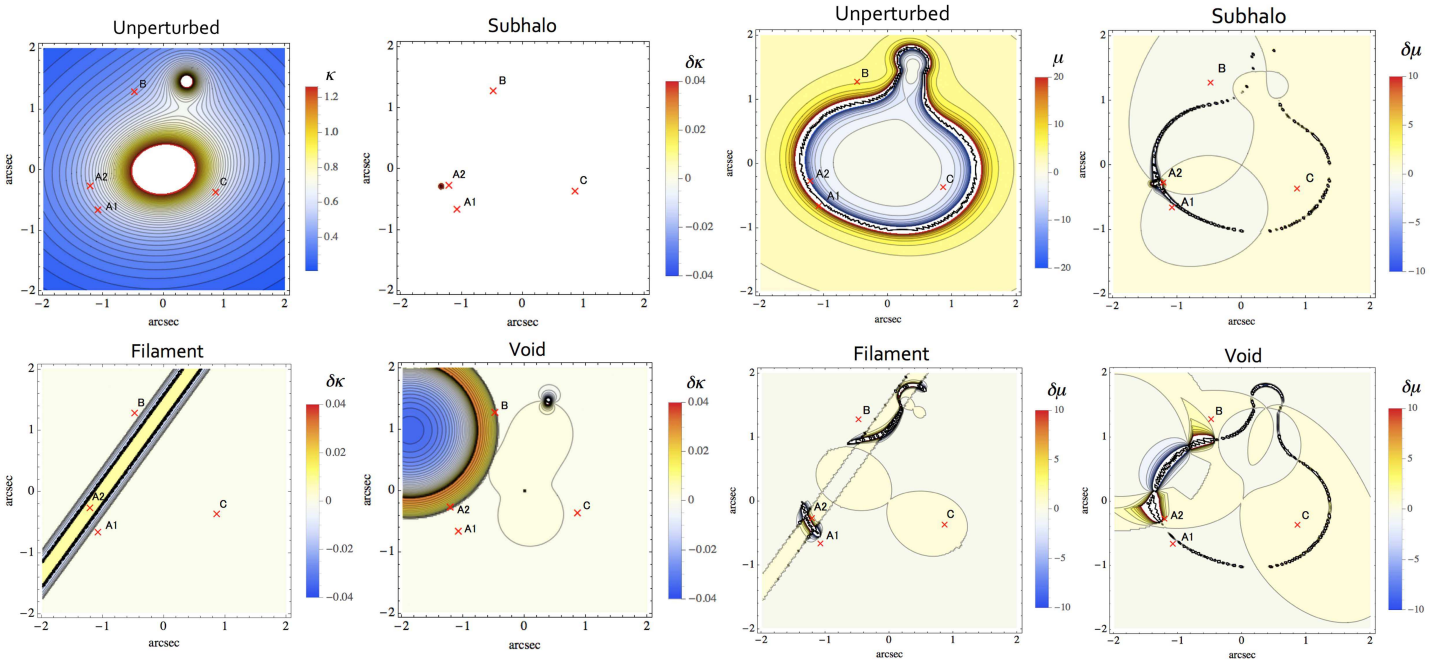


**Figure 5.** Convergence  $\kappa$  in the unperturbed model and the perturbation  $\delta\kappa$  in the best-fit perturbed models. The blank regions correspond to values outside the range shown in each accompanying legend.

**Figure 7.** Magnification  $\mu$  in the unperturbed model and the perturbation  $\delta\mu$  in the best-fit perturbed models. The blank regions correspond to values outside the range shown in each accompanying legend.

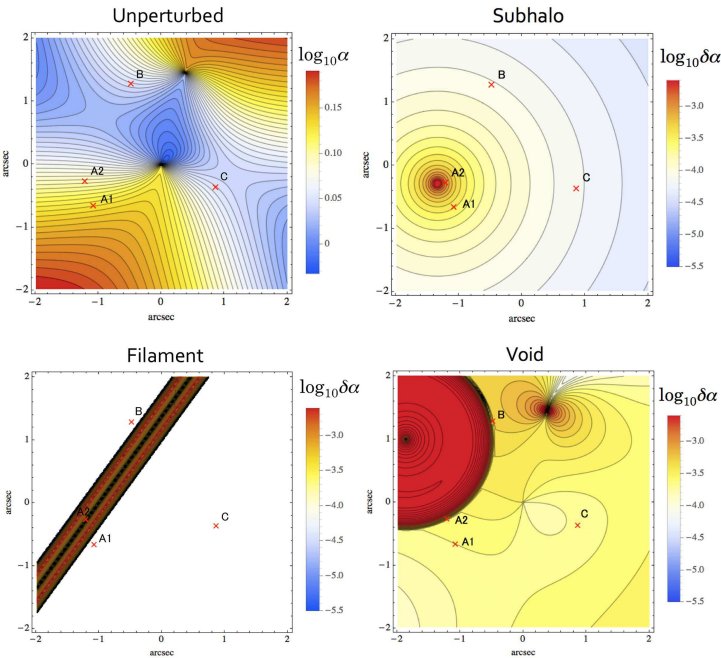


**Figure 6.** Amplitude of the deflection angle  $\alpha$  (arcsec) in the unperturbed model and the perturbation  $\delta\alpha$  (arcsec) in the best-fit perturbed models. The blank regions in the lower left panel correspond to values outside the range shown in the accompanying legend.

the anomaly in the flux ratios. Thus, observation of continuum and line emissions of MG0414+0534 in the submillimeter bands with ALMA (Atacama Large Millimeter/submillimeter Array) is of great importance to probe the origin of the flux ratio anomalies. Multifrequency observation may be necessary to break the model degeneracy.

## 6 CONCLUSION AND DISCUSSION

In this paper, we have found that the observed flux-ratio anomaly in MG0414+0534 can be explained by a presence of either a minifilament or a minivoid in the line-of-sight with a surface mass density of the order of  $10^{8-9} h^{-1} M_{\odot}/\text{arcsec}^2$  without taking into account any subhalos in the lensing galaxy. The astrometric perturbation by a possible minifilament/minivoid is  $\lesssim 0.001$  arcsec and the amplitudes of convergence perturbations due to these perturbers are typically  $\kappa \sim 0.004 - 0.008$  at the place of an image A2 that shows anomaly in the flux. In order to discriminate models with the line-of-sight ministructures from those with a subhalo(s) in the lensing galaxy, the differential magnification effect can be used if the source size is  $> 100$  pc.

In our analysis, we have used very simple models for a filament and void. They are assumed to be locally homogeneous and residing in the lens plane. We have found that all the best-fit models show that image A2 is perturbed by a perturber with a positive convergence. Although it is very important to study more realistic mass distributions for modeling the filament/void, the mass scale of possible perturber would not change much. It is also important to

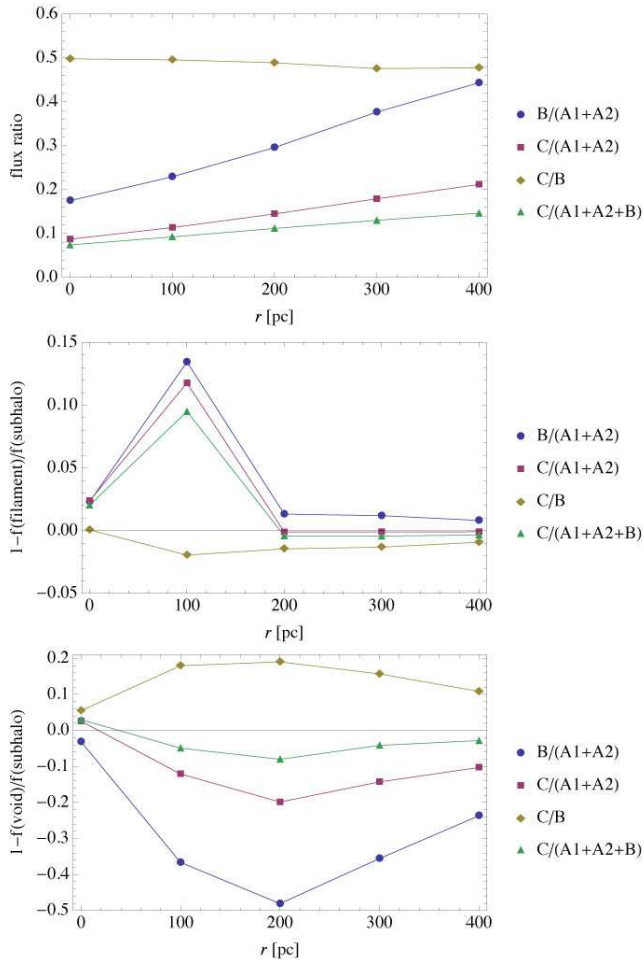


**Figure 8.** Flux ratios of the subhalo model (top), the relative differences between the filament and subhalo models (middle) and those between the void and subhalo models (bottom) as a function of the source radius  $r$ .

consider the cases in which multiple perturbers in the line-of-sight affect the lensed images. In order to do so, we need to carry out more realistic numerical simulations in which these perturbers reside at arbitrary places in the line-of-sight.

In order to break the degeneracy of possible models, we need observation at the submillimeter band using interferometers such as ALMA. If the perturber is massive enough, we may be able to directly map the gravitational perturbation by lensing (Inoue & Chiba 2003, 2005). By observing continuum and line emissions from circum-nuclear dusts around quasars at multi-frequency sub-millimeter bands, we will be able to put stringent constraints on possible models of perturbers.

Another possible way to break the model degeneracy is to use time delay of optical or near-infrared lensed images. Although the convergence perturbation around A2 are expected to be similar, the gravitational potential projected along the line-of-sight can be different in principle (McCully et al. 2014; Schneider 2014). We expect that the perturbation of time delay is conspicuous for matter distributions that are locally over-compensating since the poten-

tial wells are deep. This issue will be analyzed in detail in our future work.

If the anomaly is related to minifilaments in the line-of-sight rather than subhalos in the lensing galaxy, then we expect a correlation between perturbed fluxes of lensed images. If it is caused by subhalos, such a spatial correlation is not expected as they reside randomly in galactic halos. It is very important to assess the number of lens systems necessary for making such distinction.

Minifilaments and walls of minivoids may retain plenty of HI gas. Then HI 21-cm absorption systems in the line-of-sight would have a correlation with magnification perturbations as well as the optical-near-infrared colour due to the presence of dust. The observed HI 21-cm absorption systems at  $z = 0.3 - 0.5$  in the line-of-sight of MG0414+0534 (Tanna et al. 2013) may be connected with such minifilaments or walls. Thus, correlation study between reddening, absorption lines, and flux-ratio anomalies will be much important in near future in order to understand the clustering property of dark matter and baryons at  $\sim 10$  kpc scales.

## 7 ACKNOWLEDGMENTS

The author thanks Masashi Chiba and Ryuichi Takahashi for valuable discussion and useful comments. This work is supported in part by JSPS Grant-in-Aid for Scientific Research (B) (No. 25287062) “Probing the origin of primordial minihalos via gravitational lensing phenomena”.

## REFERENCES

- Amendola L., Frieman J. A., Waga I., 1999, *Monthly Notices of Royal Astronomical Society*, 309, 465
- Boylan-Kolchin M., Bullock J. S., Kaplinghat M., 2011, *Monthly Notices of Royal Astronomical Society*, 415, L40
- Cantalupo S., Arrigoni-Battaia F., Prochaska J. X., Hennawi J. F., Madau P., 2014, *Nature*, 506, 63
- Chen J., Kravtsov A. V., Keeton C. R., 2003, *Astrophysical Journal*, 592, 24
- Chiba M., 2002, *The Astrophysical Journal*, 565, 17
- Chiba M., Minezaki T., Kashikawa N., Kataza H., Inoue K. T., 2005, *Astrophysical Journal*, 627, 53
- Colberg J. M., Krughoff K. S., Connolly A. J., 2005, *Monthly Notices of Royal Astronomical Society*, 359, 272
- Dalal N., Kochanek C. S., 2002, *The Astrophysical Journal*, 572, 25
- Dekel A., Birnboim Y., Engel G., Freundlich J., Goerdt T., Mumcuoglu M., Neistein E., Pichon C., Teyssier R., Zinger E., 2009, *Nature*, 457, 451
- Falco E. E., Lehar J., Shapiro I. I., 1997, *Astrophysical Journal*, 113, 540
- Hewitt J. N., Turner E. L., Lawrence C. R., Schneider D. P., Brody J. P., 1992, *Astrophysical Journal*, 104, 968
- Higuchi Y., Oguri M., Shirasaki M., 2014, *Monthly Notices of Royal Astronomical Society*, 441, 745
- Inoue K. T., Chiba M., 2003, *Astrophysical Journal*, 591, L83
- Inoue K. T., Chiba M., 2005, *Astrophysical Journal*, 633, 23



- Inoue K. T., Takahashi R., 2012, *Monthly Notices of Royal Astronomical Society*, 426, 2978
- Inoue K. T., Takahashi R., Takahashi T., Ishiyama T., 2014, preprint (arXiv:1409.1326)
- Keeton C. R., Gaudi B. S., Petters A. O., 2003, *Astrophysical Journal*, 598, 138
- Klypin A., Kravtsov A. V., Valenzuela O., Prada F., 1999, *Astrophysical Journal*, 522, 82
- Koopmans L. V. E., Biggs A., Blandford R. D., Browne I. W. A., Jackson N. J., Mao S., Wilkinson P. N., de Bruyn A. G., Wambsganss J., 2003, *The Astrophysical Journal*, 595, 712
- Kormann R., Schneider P., Bartelmann M., 1994, *Astronomy and Astrophysics*, 284, 285
- Lawrence C. R., Elston R., Januzzi B. T., Turner E. L., 1995, *Astronomical Journal*, 110, 2570
- McKean J. P., Koopmans L. V. E., Flack C. E., Fassnacht C. D., Thompson D., Matthews K., Blandford R. D., Readhead A. C. S., Soifer B. T., 2007, *Monthly Notices of the Royal Astronomical Society*, 378, 109
- MacLeod C. L., Jones R., Agol E., Kochanek C. S., 2013, *The Astrophysical Journal*, 773, 35
- Mao S., Schneider P., 1998, *Monthly Notices of the Royal Astronomical Society*, 295, 587
- Martin D. C., Chang D., Matuszewski M., Morrissey P., Rahman S., Moore A., Steidel C. C., Matsuda Y., 2014, *Astrophysical Journal*, 786, 107
- McCully C., Keeton C. R., Wong K. C., Zabludoff A. I., 2014, *Monthly Notices of Royal Astronomical Society*, 443, 3631
- Mead J. M. G., King L. J., McCarthy I. G., 2010, *Monthly Notices of Royal Astronomical Society*, 401, 2257
- Metcalf R. B., 2005, *The Astrophysical Journal*, 629, 673
- Metcalf R. B., Madau P., 2001, *The Astrophysical Journal*, 563, 9
- Metcalf R. B., Moustakas L. A., Bunker A. J., Parry I. R., 2004, *Astrophysical Journal*, 607, 43
- Minezaki T., Chiba M., Kashikawa N., Inoue K. T., Kataza H., 2009, *Astrophysical Journal*, 697, 610
- Moore B., Ghigna S., Governato F., Lake G., Quinn T., Stadel J., Tozzi P., 1999, *Astrophysical Journal*, 524, L19
- More A., McKean J. P., More S., Porcas R. W., Koopmans L. V. E., Garrett M. A., 2009, *Monthly Notices of the Royal Astronomical Society*, 394, 174
- Navarro J. F., Frenk C. S., White S. D. M., 1996, *Astrophysical Journal*, 462, 563
- Planck Collaboration Ade P. A. R., Aghanim N., Armitage-Caplan C., Arnaud M., Ashdown M., Atrio-Barandela F., Aumont J., Baccigalupi C., Banday A. J., et al. 2013, preprint, arXiv:1303.5062
- Ros E., Guirado J. C., Marcaide J. M., Perez-Torres M. A., Falco E. E., Munoz J. A., Alberdi A., Lara L., 2000, *Astronomy and Astrophysics*, 362, 845
- Schechter P. L., Moore C. B., 1993, *Astronomical Journal*, 105, 1
- Schneider P., 2014, preprint(arXiv:1409.0015)
- Simon J. D., Bolatto A. D., Leroy A., Blitz L., Gates E. L., 2005, *Astrophysical Journal*, 621, 757
- Sugai H., Kawai A., Shimono A., Hattori T., Kosugi G., Kashikawa N., Inoue K. T., Chiba M., 2007, *Astrophysical Journal*, 660, 1016
- Sutter P. M., Lavaux G., Wandelt B. D., Weinberg D. H., Warren M. S., Pisani A., 2014, *Monthly Notices of Royal Astronomical Society*, 442, 3127
- Swaters R. A., Madore B. F., van den Bosch F. C., Balcells M., 2003, *Astrophysical Journal*, 583, 732
- Takahashi R., Inoue K. T., 2014, *Monthly Notices of Royal Astronomical Society*, 440, 870
- Tanna A., Curran S. J., Whiting M. T., Webb J. K., Bignell C., 2013, *Astrophysical Journal*, 772, L25
- Tonry J. L., Kochanek C. S., 1999, *Astronomical Journal*, 117, 2034
- Trotter C. S., Winn J. N., Hewitt J. N., 2000, *Astrophysical Journal*, 535, 671
- Wang J., Frenk C. S., Navarro J. F., Gao L., Sawala T., 2012, *Monthly Notices of Royal Astronomical Society*, 424, 2715
- Xu D., Mao S., Wang J., Springel V., Gao L., White S., Frenk C., Jenkins A., Li G., Navarro J., 2009, *Monthly Notices of the Royal Astronomical Society*, 398, 1235
- Xu D. D., Mao S., Cooper A. P., Gao L., Frenk C. S., Angulo R. E., Helly J., 2012, *Monthly Notices of the Royal Astronomical Society*, 421, 2553
- Xu D. D., Mao S. D., Cooper A. P., Wang J., Gao L. A., Frenk C. S., Springel V., 2010, *Monthly Notices of the Royal Astronomical Society*, 408, 1721